

Central Lancashire Online Knowledge (CLoK)

Title	Toroidal ordering of artificial magnetic systems by spontaneous symmetry
	breaking
Type	Article
URL	https://knowledge.lancashire.ac.uk/id/eprint/57243/
DOI	https://doi.org/10.1103/lbx1-hrdd
Date	2025
Citation	Tóbik, Jaroslav, Bokes, Peter, Lepadatu, Serban, Vetrova, Iuliia, Ščepka, Tomáš and Šoltýs, Ján (2025) Toroidal ordering of artificial magnetic systems by spontaneous symmetry breaking. Physical Review B, 112 (13). ISSN 2469-9950
Creators	Tóbik, Jaroslav, Bokes, Peter, Lepadatu, Serban, Vetrova, Iuliia, Ščepka, Tomáš and Šoltýs, Ján

It is advisable to refer to the publisher's version if you intend to cite from the work. https://doi.org/10.1103/lbx1-hrdd

For information about Research at UCLan please go to http://www.uclan.ac.uk/research/

All outputs in CLoK are protected by Intellectual Property Rights law, including Copyright law. Copyright, IPR and Moral Rights for the works on this site are retained by the individual authors and/or other copyright owners. Terms and conditions for use of this material are defined in the http://clok.uclan.ac.uk/policies/

Toroidal ordering of artificial magnetic systems by spontaneous symmetry breaking

Jaroslav Tóbik, ^{1,*} Peter Bokes, ² Serban Lepadatu, ³ Iuliia Vetrova, ¹ Tomáš Ščepka, ¹ and Ján Šoltýs ¹ Institute of Electrical Engineering, Slovak Academy of Sciences,

Dúbravská cesta 9, SK-841 04 Bratislava, Slovakia

² Institute of Nuclear and Physical Engineering, Faculty of Electrical Engineering,

Slovak University of Technology in Bratislava, Ilkovičova 3, SK-841 04 Bratislava, Slovakia

³ Jeremiah Horrocks Institute, University of Central Lancashire, Preston PR1 2HE, UK

(Dated: October 23, 2025)

The new magnetization protocol is proposed for structures with magnetic ferrotoroidal order as the ground state. The structures should be magnetized by an out-of-plane magnetic field until saturation first; then the out-of-plane magnetic field is slowly turned off. During the demagnetization process from saturation, a series of spontaneous symmetry breaking events occur. These symmetry breaking events create new meta-stable states at lower fields. The ferrotoroidal state is stable after the first spontaneous symmetry breaking, and it remains the lowest energy state during the switching off of the external magnetic field. The out-of-plane field thus not only lowers the barriers among states but also destabilizes the higher-energy metastable states of the artificial crystal unit cell, changing the free-energy map of the system qualitatively. This protocol is studied analytically within the macrospin model, numerically on a realistic structure, and is realized experimentally. Switching from non-toroidal to toroidal order is demonstrated on isolated magnetic sub-micrometer structures as well as on arrays of such structures.

I. INTRODUCTION

The development of technology enables the fabrication of artificial structures on a sub-micrometer scale with a high degree of definition of building elements. The periodic repetition of the patterned elements defines a crystal. Thus, technology enables us to create artificial materials with properties that are not found in natural materials. The typical examples are metamaterials[1, 2] materials intentionally designed to have a negative refraction index for electromagnetic waves in some frequency range. In the field of applied magnetism, there is vivid research in artificial structurally periodic arrays of magnetic elements. The special class of magnetic materials is materials with ferrotoroidal order. Ferrotoroidal order is characterized by magnetization forming closed loops within the unit cell. Ferrotoroidal phase breaks both space and time inversion symmetry, opening the possibility for many technologically interesting phenomena to occur[3-6]. In this paper, we study an artificial structure with a square lattice and the ferrotoroidal ground state. Our motivation to study this structure is the prediction that unidirectional edge states might exist in such a crystal[7]. A technologically achievable structure with measurable bandwidth was theoretically calculated [8]. It is of notable interest to fabricate and prepare such structures with the desired ferrotoroidal magnetic state.

However, artificial magnetic structures usually have a nonperiodic magnetic pattern. There are numerous reasons for difficulties in achieving magnetic order. The main obstacle is the presence of many local minima and large energy barriers among them. The energy barriers are usually much higher than the achievable thermal energy. Therefore, thermally activated magnetization flipping is possible only during the growth process [9–12] when the thickness of the magnetic material is about 1 nm. Then, the magnetic structure freezes. The magnetic state manipulation afterwards is problematic, especially in cases where the ground state has no net magnetization, as in the case of ferrotoroic order. The domain structure is determined by the strength of the interaction of the nearest neighbors, which in turn is determined by the geometry of the sample [11, 13]. Another approach is to heat up the sample over the Curie temperature of the constituting ferromagnetic material and anneal the sample[14]. With this approach, spontaneous ferrotoroic ordering was observed as a function of the interaction of constituting elements defined by their separation. The long range order in this approach is possible for strongly interacting elements.

The circular arrangement excludes control of the toroid magnetic moment with a homogeneous external magnetic field due to symmetry. It was demonstrated experimentally that it is possible to control the circulation of microscopic units via a localized magnetic field produced by, for example, the magnetic tip used in magnetic force microscopy[10, 15]. However, setting each unit cell in the crystal individually using this method is a laborious and a time-consuming method. The strength of the magnetic tip is also a limiting factor, since there are limits given by the element's shape anisotropy and by interactions with neighboring magnetic elements.

Another possibility is to optimize the design of magnetic building blocks with [16], or without [17] lowered spatial symmetry of the artificial structure.

To reach ferrotoroidal order, we suggest a new type of magnetic protocol. First, we magnetize the sample by an out-of-plane field until saturation. The sample should be

^{*} jaroslav.tobik@savba.sk

saturated to a unique out-of-plane magnetic state. The consequent reduction of the out-of-plane magnetic field keeps the system in a unique magnetic state up to the critical field value. At this magnetic field, the system reaches a spontaneous symmetry breaking instability at which the unit cells start to evolve a ferrotoroidal moment. At the magnetic field below, but close to the critical field, the temperature is still able to synchronize adiacent unit cells via thermally activated barrier crossing. Reducing the external out-of-plane magnetic field causes further rotation of magnetic moments to an in-plane direction and increases energy barriers between states of different in-plane circulation. The successive decrease of the out-of-plane magnetic field eventually stabilizes other metastable states (e.g., onion state). Still, these states are higher in energy, and some energy barrier is needed to be thermally overcome to spoil the toroidal order.

The structure of the paper is as follows: in the next section "Experiment", we present experimental results when fabricated structures were magnetized by an inplane field to the so-called onion states, and then our protocol of an out-of-plane field was applied. Then the evolution of the ferrotoroidal order is explained using the analytically treatable macrospin model in the third section "Macrospin Model". Next, the conceptual findings of the macrospin model are confirmed by more complex micromagnetic calculations in the section "Micromagnetic Calculations". Within the micromagnetic model, we computed the free-energy potential maps as a function of the external out-of-plane magnetic field. Finally in the section "Effects of Imperfections" we discuss problems faced in ordering arrays in ferrotoroidal order.

II. EXPERIMENT

Artificial magnetic structures were patterned using electron beam lithography (EBL) and positive tone resist PMMA 950K. The resist was spread by spin coating on a silicon substrate, then baked on a hotplate at a temperature of 175 °C for 5 minutes. In order to achieve 30-nm gaps between patterns, we thinned the original resist with chlorobenzene, which at a speed of 5000 rpm resulted in a film thickness of about 50 nm. The triangle patterns were generated using 30 kV e-beam and beam current of 40 pA. The optimal exposure dose varies in the range of $300-400 \ \mu C/cm^2$. Then the development at a temperature of 6 °C in a MIBK:IPA (1:3) solution for 75 seconds was applied. Cold development can improve the overall quality of the patterns, making them more precise and well-defined [18]. Next, a 20-nm-thick layer of permalloy (Py) was e-gun evaporated from Ni80Fe20 source. Subsequently, the standard lift-off technique in acetone was performed to reveal patterned structures. Fig. 1 shows the fabricated single Pv squares, each with a 400 nm side and composed of four individual triangles separated by a 30 nm gap, as well as a 10x10 array of these squares.

The final sample was magnetized using a Weiss-type

electromagnet. First, an in-plane external magnetic field of 0.5 T was applied diagonally along squares. The magnetic state of the sample was investigated by a magnetic force microscope (MFM) at room temperature with the standard two-pass semicontact MFM technique. The lift distance in the second pass was 30 nm. Measurements were made with a super-sharp SSS probe (NANOSEN-SOR) that has a low magnetic moment and coercivity $(\sim 0.25 \times 10^{-13} \text{ emu and } 125 \text{ Oe})$ to achieve high spatial resolution and not affect the magnetic states of the structures. Although the first pass provided topography (Fig. 2.A), the second pass revealed that the magnetization in all unit cells was oriented into the so-called "onion state" during in-plane magnetization (Fig. 2.B). Then, we applied an out-of-plane external magnetic field of 0.94 T to ensure that the magnetic structure reached magnetization saturation. After a gradual decrease of the field over 10 minutes, the magnetization states of the structures were re-evaluated by MFM (Fig. 2.C). In the case of the isolated squares, all squares except one are in a circular state. In the case of an array of squares, two domain walls are formed, dividing the squares into domains with the same circulation of magnetization.

III. MACROSPIN MODEL

To understand the undergoing process, we study the basic unit cell of an artificial magnetic crystal by a macrospin model approximation. This unit cell is made up of square cut diagonally into four isosceles triangles (see Fig. 1). The simple and analytically treatable model for the unit cell is four macrospins with magnetic moment m. The macrospins mutually interact via magnetostatic interaction. The triangular isosceles elements have elongated shapes, which is taken into account by the shape anisotropy term. The model assumes only the nearestneighbor interaction based on the dipole-dipole interaction. The notation and coordinate orientation follow the Fig. 1. The shape anisotropy and dipole-dipole energies can be expressed via matrices, which is very convenient for algebraic manipulation in further analysis. For this purpose, we introduce the 12-dimensional linear space for the magnetization vector μ as a direct product of 4 linear spaces where the 3-dimensional vectors $\mathbf{m}_1, ..., \mathbf{m}_4$ are defined. Using this construction, the total energy of the system of 4 interacting dipoles can be expressed as the following:

$$E = \boldsymbol{\mu} \cdot \boldsymbol{\mathcal{H}} \cdot \boldsymbol{\mu} - \boldsymbol{\mu} \cdot \mathbf{B}$$

$$\mathcal{H} = \begin{pmatrix} \mathcal{A}_{x} & \mathcal{J}_{++} & 0 & \mathcal{J}_{+-} \\ \mathcal{J}_{++} & \mathcal{A}_{y} & \mathcal{J}_{+-} & 0 \\ 0 & \mathcal{J}_{+-} & \mathcal{A}_{x} & \mathcal{J}_{++} \\ \mathcal{J}_{+-} & 0 & \mathcal{J}_{++} & \mathcal{A}_{y} \end{pmatrix}.$$

$$(1)$$

The 3×3 matrices \mathcal{J}_{++} , \mathcal{J}_{+-} represents dipole-dipole interactions of two dipoles along two different orientations in space (see Fig. 1). The matrices \mathcal{A}_x , \mathcal{A}_y express the shape anisotropy when only the largest value is taken

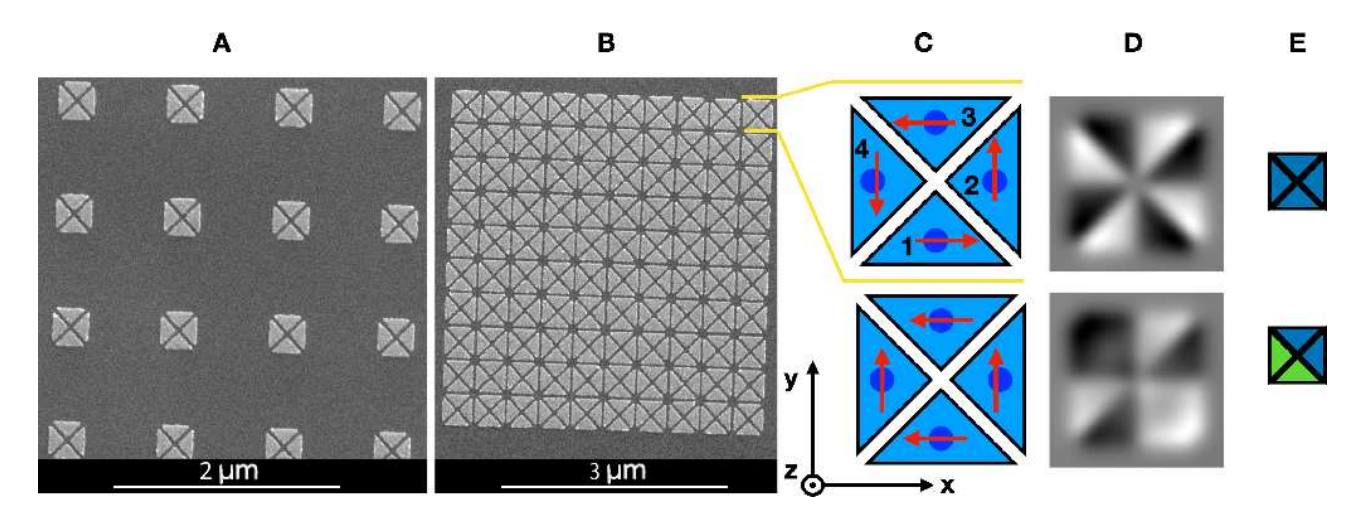


FIG. 1. SEM image of the isolated magnetic structures (panel A), arrays of such structures (panel B) and macrospin model of the single unit cell (panel C). The orientation of axes and numbering of macrospins are according the analytical model discussion. Calculated MFM images of circular (top) and onion (bottom) states are shown in panel D. Panel E shows color code for magnetization orientation used later in domain structure vizualization. Clockwise orientation is coded green, counterclockwise blue.

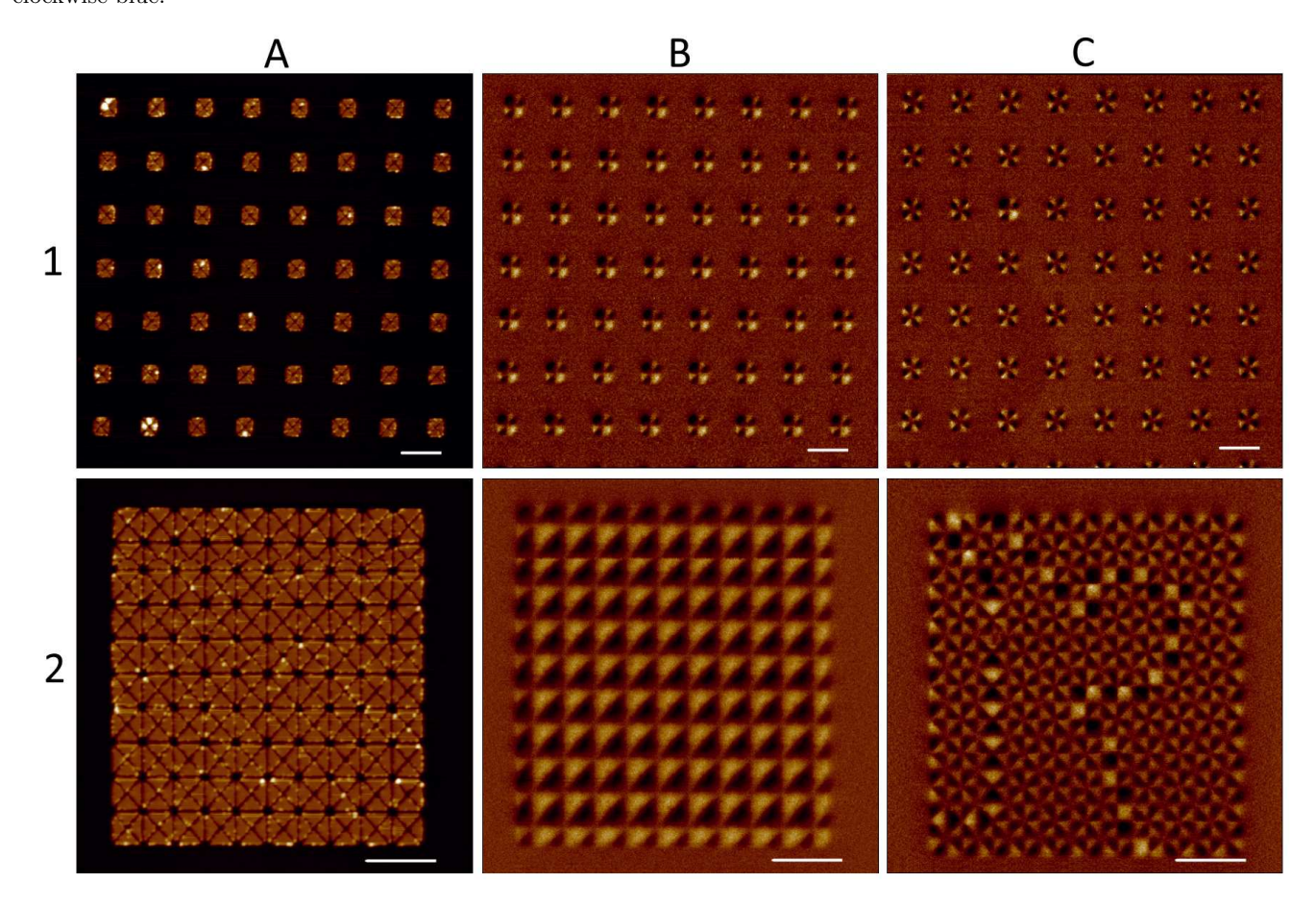


FIG. 2. MFM images of (1) isolated single unit cells and (2) an array of 10x10 elements. A column shows topography, B column shows the magnetic states after applying an in-plane external magnetic field of 0.5 T along the squares diagonal, C column shows magnetic states after applying an out-of-plane magnetic field of 0.937 T. The white bar in the bottom right corner of the images evaluates 1 μ m size.

into account. The largest value is in the direction along the longest edge of the isosceles triangle.

$$\mathcal{J}_{++} = \begin{pmatrix}
-J & -3J & 0 \\
-3J & -J & 0 \\
0 & 0 & 2J
\end{pmatrix}, \quad \mathcal{J}_{+-} = \begin{pmatrix}
-J & 3J & 0 \\
3J & -J & 0 \\
0 & 0 & 2J
\end{pmatrix}$$

$$\mathcal{A}_{x} = \begin{pmatrix}
-A & 0 & 0 \\
0 & 0 & 0 \\
0 & 0 & 0
\end{pmatrix}, \quad \mathcal{A}_{y} = \begin{pmatrix}
0 & 0 & 0 \\
0 & -A & 0 \\
0 & 0 & 0
\end{pmatrix} \tag{2}$$

Irred. Rep. Eigenvalue(s)
$$\begin{array}{lll}
A_1 & \lambda_1 = 4J, \ \lambda_2 = 6J \\
B_1 & \lambda_3 = -6J, \ \lambda_4 = -4J \\
A_2 & \lambda_5 = -A - 6J \\
B_2 & \lambda_6 = -A + 6J \\
E & \lambda_7 = \lambda_8 = (-A - \sqrt{A^2 + 16J^2})/2 \\
\lambda_9 = \lambda_{10} = (-A + \sqrt{A^2 + 16J^2})/2 \\
\lambda_{11} = \lambda_{12} = 0
\end{array}$$

TABLE I. Eigenvalues of dipole-dipole matrix \mathcal{H} . Eigenvectors are shown on Fig. 3.

Where $J = \frac{\mu_0 |\mathbf{m}|^2}{16\pi a^3}$, μ_0 is permeability of vacuum, a distance of nearest-neighbour macrospins.

Next, assume that the homogeneous external field is applied in the z direction following the notation in Fig. 1. The symmetry group of the energy function (1), including also the non-zero external field, is C_{4v} . The dipole-dipole interaction matrix \mathcal{H} in Eq. (1) can be block diagonalized with the use of symmetry and group theory[19]. Consequently, individual blocks can be completely analytically diagonalized. Almost all eigenvectors are independent of interaction constants A and J, except for vectors in the plane belonging to irreducible representation E. The eigenvalues of the \mathcal{H} matrix are listed in the Tab. I and corresponding eigenvectors \mathbf{e}_1 to \mathbf{e}_{12} are shown in Fig.3 [20].

The homogeneous external magnetic field ${\bf B}$ oriented in the z direction is expressed as ${\bf B}=B{\bf e}_1$. In Eq. (1), the vector ${\boldsymbol \mu}$ is constrained to have amplitude $|{\boldsymbol \mu}|^2=4$. As a result, the quadratic term is bounded, and the linear term can be arbitrarily large by increasing the magnitude of B. Starting from the limit of large B in Eq. (1), the linear term in ${\boldsymbol \mu}$ is dominant and the system has a unique minimum ${\boldsymbol \mu}={\bf e}_1$. The energy of the system (1) is then:

$$E = 4\lambda_1 - 4B. (3)$$

As the external field B decreases, the energy E given by Eq.(3) can be further minimized, allowing μ to also have component with the lowest eigenvalue of the dipole-dipole interaction, which is in this case the direction \mathbf{e}_5 . The μ can be parametrized:

$$\boldsymbol{\mu} = \sqrt{1 - \epsilon^2} \, \mathbf{e}_1 + \epsilon \, \mathbf{e}_5 \tag{4}$$

The ϵ parameter is amplitude of \mathbf{e}_5 component in $\boldsymbol{\mu}$ vector. The parametrization (4) preserves subsidiary conditions $|\mathbf{m}_i|^2 = 1$. Putting this parameterization into Eq. (1) gives:

$$E = 4(1 - \epsilon^2)\lambda_1 + 4\epsilon^2\lambda_5 - 4B\sqrt{1 - \epsilon^2}$$
 (5)

Using standard calculus we find that for $B > B_c = 2(\lambda_5 - \lambda_1)$ the minimum is $\epsilon = 0$, but for $B < B_c$ there are two equivalent minima $\epsilon = \pm \sqrt{1 - \frac{B^2}{4(\lambda_5 - \lambda_1)^2}}$. The same procedure can be performed with other modes in the plane, but since λ_5 is the smallest eigenvalue of the

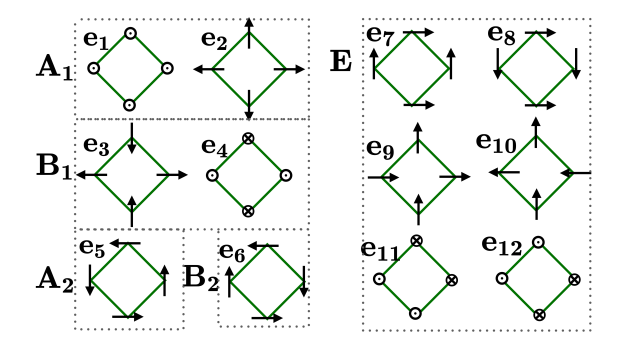


FIG. 3. Symmetry adapted base for 4 macrospin model with C_{4v} symmetry group. Arrows represent magnetic moments of individual macrospins, green lines are eye-guides showing nearest-neighbour interactions. Base 12-dimensional vectors e_1, \dots, e_{12} are chosen according this figure, irreducible representations are noted by capital letters A_1, \dots, E

matrix \mathcal{H} , \mathbf{e}_5 is the first direction of spontaneous symmetry breaking. So, the system randomly chooses one of the two minima, and due to the fact that these states minimize the pair interaction matrix \mathcal{H} it remains the global minimum of the system when the external field B is lowered further.

Consider now the unit cells at the magnetic field where only the toroidal magnetic states are stable. If we put these unit cells into an array with weak interaction, we get a two-dimensional Ising model. As the interaction among unit cells becomes stronger, it can stabilize a state other than the toroidal state in the unit cell again. Such a state is higher in energy, but can be a local minimum of the energy. In fact, previously it was shown that the ratio of inter-cell and intra-cell interactions changes the type of domain walls[11]. It was also qualitatively shown that the largest ferrotoroidal domains are achieved if the intra- and inter-cell interaction strengths are of comparable strength.

IV. MICROMAGNETIC CALCULATIONS

In order to show that general features of the macrospin model are valid for the more realistic model, we computed the energy barriers that separate the different magnetic configurations of the artificial spin crystal unit cell. A parallel version of the metadynamics algorithm[21–23] was developed within a micromagnetic model, based on the tempered metadynamics algorithm [24]. The metadynamics algorithm was implemented within the BORIS[25, 26] software, using the micromagnetic Monte Carlo method (MMC)[27]. The MMC method uses a compound trial move consisting of magnetization rotation and length change based on the Maxwell-Boltzmann distribution, with trial move acceptance probability given as:

$$P_{acc}(A \to B) = \min \left\{ 1, \frac{m_B^4}{m_A^4} \exp \left(-\frac{\Delta F + \Delta V}{k_B T} \right) \right\} (6)$$

Here, $\mathbf{m}_{A(B)} = \mathbf{M}_{A(B)}/M_{S0}$ is the magnetization vector normalized to zero-temperature saturation magnetization, and $\Delta F = F(\mathbf{m}_B) - F(\mathbf{m}_A)$ is the change in total free energy from initial state A to trial state B. A metadynamic potential V is computed, and the additional energy cost of trial moves is included as $\Delta V = V_B - V_A$. The free energy function in this work, $F = F_{ex} + F_d + F_{Zee}$, includes contributions from exchange interaction, magnetostatic interaction, and external field, respectively.

The metadynamics potential V is computed in BORIS using a general-purpose implementation, allowing user-defined collective variables $Q_i(i=1,2,3)$ for 1D, 2D, and 3D versions of the algorithm, respectively. The 2D metadynamics potential is defined

$$V(Q_{1}, Q_{2}, t) = V_{0} \sum_{t_{i} < t} \exp \left[-\frac{V(Q_{1}, Q_{2}, t_{i})}{k_{B} \Delta T} \right]$$

$$\exp \left[-\left(\frac{Q_{1}(t_{i}) - Q_{1}(t)}{\sigma_{Q_{1}}} \right)^{2} - \left(\frac{Q_{2}(t_{i}) - Q_{2}(t)}{\sigma_{Q_{2}}} \right)^{2} \right]$$
(7)

where V_0 is a set amplitude, ΔT is the tempering temperature, and σ_{Qi} are decay widths of the respective collective variables. In Eq. (7), the sum runs over all previously computed iterations, where $Q_1(t_i)$, $Q_2(t_i)$ are collective variables calculated at actual configuration at time t_i . Computationally, a discrete collective variable grid is defined, and at the end of each Monte Carlo iteration, the metadynamic potential is updated in each (Q_1,Q_2) grid cell by adding a new exponential term contribution using the latest collective variable values $Q_i(t)$. Moreover, when computing the metadynamics potential energy change, $\Delta V = V_B - V_A$, the V values are obtained using bilinear interpolation in the (Q_1, Q_2) grid. In Ref. [23] a serial metadynamics algorithm was used. To allow large-scale computations, a parallel implementation of the metadynamics algorithm was introduced in BORIS, running on graphical processing units (GPU), for single and multiple GPUs [28]. In order to avoid data races, the values of the collective variables $Q_i(t)$ are not updated after an accepted trial move, and instead are updated at the end of each Monte Carlo iteration. The finite difference magnetization grid is decomposed using the red-black checkerboard scheme discussed previously [29]. As tested, computations using serial and parallel versions of the algorithm result in the same computed metadynamics potential.

In this work the collective variables used are the magnetic in-plane vorticity, Eq. (8), with values ranging from -1 to +1, and deviation from vorticity, Eq. (9), with val-

ues ranging from 0 to +1:

$$Q_1 = \frac{1}{N} \sum_{i=1}^{N} (\hat{\mathbf{r}}_{xy,i} \times \hat{\mathbf{m}}_i) \cdot \hat{\mathbf{z}}$$
 (8)

$$Q_2 = \frac{1}{N} \sum_{i=1}^{N} 1 - [(\hat{\mathbf{r}}_{xy,i} \times \hat{\mathbf{m}}_i) \cdot \hat{\mathbf{z}}]^2.$$
 (9)

In the above equations, $\hat{\mathbf{r}}_{xy,i}$ is the unit direction vector from the vortex center to the *i*-th computational cell, $\hat{\mathbf{m}}_i$ is the unit magnetization direction vector in the *i*-th computational cell, where the sum runs over all N computational cells. For the artificial spin ice unit cell in Fig. 1, the vortex center is defined at the center of the unit cell, such that Q_1 values of ± 1 correspond to perfectly circular vortices with anticlockwise, respectively clockwise, circulation. Values of ± 0.5 correspond to one of the triangle magnetization directions flipped away from the anticlockwise, respectively clockwise, circulation, with 4 degenerate configurations possible. Finally, values of 0 correspond to an equal split of anticlockwise and clockwise circulation between the magnetization directions of the 4 triangles, with 6 degenerate configurations possible.

The metadynamic potential was computed as a function of the external field for the artificial spin ice unit cell of Fig. 1, with the experimentally realized dimensions of $400 \times 400 \times 20$ nm and the 30 nm gap between triangles. The potential was calculated at room temperature for the $Ni_{80}Fe_{20}$ material with $M_{S0}=800$ kA/m, $A_0=13$ pJ/m, and Curie temperature $T_C=870$ K, using a 5 nm cellsize. The temperature-dependent saturation magnetization is $M_S(T)=M_S^0m_e(T)$, and the temperature-dependent exchange stiffness is $A(T)=A_0m_e^2(T)$, where $m_e(T)=B[m_e3T_C/T+h^3M_{S0}\mu_0H_{ext}/k_BT]$ is the equilibrium magnetization scaling function, with B(x)=coth(x)-1/x. For the metadynamics potential function of Eq. (7), $V_0=1eV$, $\sigma_{Q1}=\sigma_{Q2}=0.01$, and $\Delta T=10^6K$, which was converged over 250×10^6 iterations.

The resultant potential energy (which is the negative of the computed metadynamics potential) is shown in Fig. 4 for zero external field. Five local energy minima are identified, corresponding to the five sets of degenerate magnetic configurations indicated by the diagrams. Due to the shape anisotropy of the triangles, resulting in magnetization vectors aligning with the edges, the ideal vorticity values of $\pm 1, \pm 0.5$ are reduced as observed in Fig. 4.

The local energy minima are also shown in Fig. 4 as a function of Q_1 , obtained as minimum energy paths through the computed potential energy map. It can be seen that the circulating vortex states have the lowest energy, whilst the other 3 states are stabilized as local energy minima in zero field, separated by energy barriers. At room temperature and with zero external field, the energy barriers effectively result in a frozen magnetic configuration. However, as the out-of-plane field is increased, it can be seen that the energy barriers separating

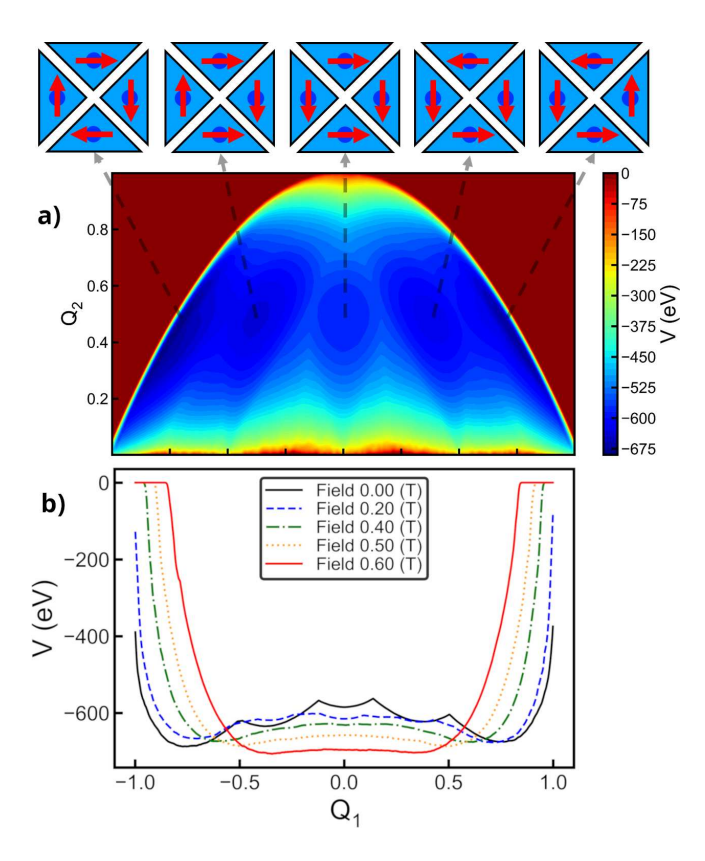


FIG. 4. Panel a): numerically computed potential energy map as a function of collective variables Q1, Q2 (Eqs.(8), (9)). The map is computed in zero field for a unit cell, with example configurations identified using the unit cell diagrams. Panel b): minimum energy paths obtained from computed potential energy maps with varying out-of-plane magnetic field, showing the reduction in energy barriers between the 5 sets of degenerate magnetic configurations.

these states are gradually reduced, and eventually only the circulating vortex states remain as energy minima. Further increasing the field removes this final energy barrier, allowing for transitions between the clockwise and anticlockwise circulations, as can be seen in Fig. 4 for the 0.6T field. Thus, it is expected that upon gradual reduction of the out-of-plane field from saturation, the resulting magnetic configuration of an artificial spin ice array will consist largely of circulating vortex states with a mixture of clockwise and anticlockwise vorticities.

We also performed a simulation of the ordering process of the 10×10 array using the standard Monte Carlo algorithm at room temperature. The gradual reduction of the out-of-plane field from 1.0 T to 0.0 T was applied with the field reduction speed at a rate of 0.01 T per 2×10^4 Monte Carlo iterations. . The resulting magnetic configuration is shown in Fig. 5. As expected, the vast majority of unit cells are found in a circulating vortex state, but mono-domain ferrotoroidal structure was not achieved.

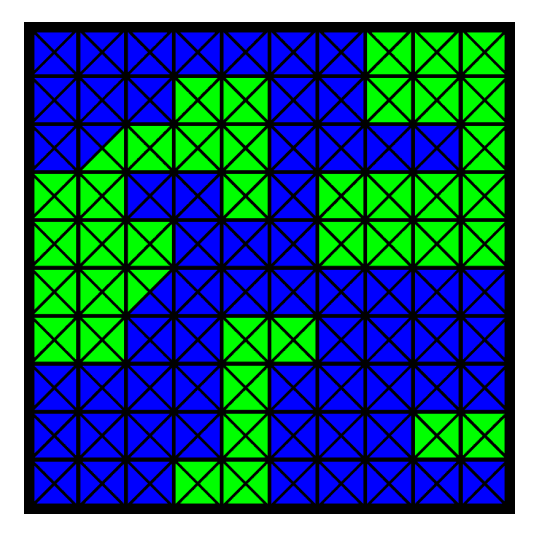


FIG. 5. Ferrotoroidal domain structure as the result of Monte Carlo simulation of a 10 by 10 unit cell array at T=300K, with ideal geometry and perfect external field alignment. Color coding follows notation in Fig. 1E - clockwise rotation is shown in green, counterclockwise in blue.

V. EFFECTS OF IMPERFECTIONS

Real-world experiments are always influenced by pervasive imperfections. As already shown in Fig. 2, we did not find a ferrotoroidal monodomain. We obtained some domain structure within arrays of 10 by 10 unit cells. We had several such arrays fabricated on our sample, and the domain structure of the other arrays is shown in Fig. 6. In order to show magnetic order in a more easily readable form, we color-coded the magnetic order of individual elements in blue-green maps. The colors reflect a positive or negative contribution to the toroidal moment of every particular element.

There are multiple reasons for the existence of domains. First, it is the finite temperature during the experiment that prevents the physical system from reaching the ground state in favor of higher entropy. The second reason is the finite time that we have available for the annealing of the samples. Our magnetization protocol was performed in minutes. These two factors are unavoidable even in experiments with a geometrically perfect sample. To demonstrate this effect, a 10×10 array of the artificial spin ice unit cell was simulated using the standard Monte Carlo algorithm at room temperature, with gradual reduction of the out-of-plane field from 1.0 T down to 0.0 T. The resulting magnetic configuration is shown in Fig. 5, where the field was decreased at a rate of 0.01 T per 2×10^4 Monte Carlo iterations.

Another problem is the effect of the misalignment of the external magnetic field[30]. Indeed, if we look at the shape of symmetry adapted base vectors of Fig. 3, the base vectors belonging to the irreducible representation of E couple to the in-plane homogeneous magnetic field. Zeeman term might lower the energy of some state

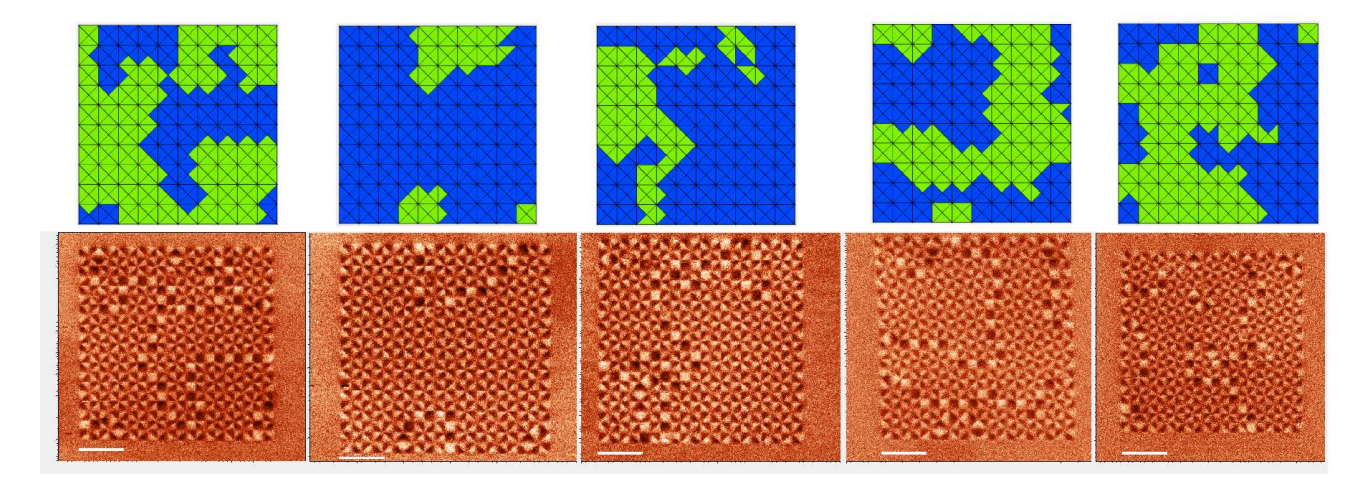


FIG. 6. Ferrotoroidal domain structure of various arrays composed of 10x10 unit cells grown on the same sample. MFM images are on bottom line, graphical interpretation of ferro-toroidal order on the top line. $1\mu m$ scale bar is show in each MFM scan by white line.

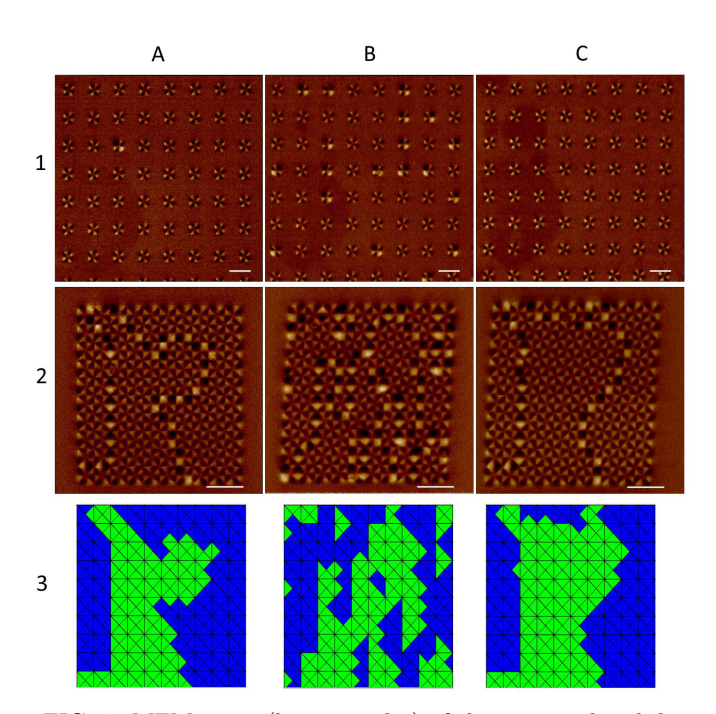


FIG. 7. MFM scans (lines 1 and 2) of the same isolated dots (line 1) and 10x10 array (line 2) after successive out of plane re-magnetization. Line 3 shows simplified vizualization of the fero-toroidal order of the arrays on line 2. Columns A and C shows good alignment of the sample during the magnetization protocol, column B indicates presence of the in-plane field during magnetization.

belonging to the irreducible representation E below the chiral state of the symmetry A_2 . In Fig.7 we show a sequence of out-of-plane magnetization results of the same 10 by 10 array. As there is an in-plane field component present, the isolated dots are not in toroidal state (column B) only, but a significant population of onion states is visible. Magnetic states of isolated dots are good indi-

cators of the in-plane field presence.

Another source of real-world imperfection is structural disorder. The fabricated structures are not identical because of technological limits. It is well known that shape asymmetry can induce a preference for a particular state in otherwise degenerate states [31, 32]. In this sense, our structures are sensitive to imperfections in the out-ofplane direction. In fact, the lift-off fabrication technology we used might introduce protrusions on the edges of the fabricated structures. Structures having inversion symmetry should not have a preference for some particular toroidal state, but imperfections might introduce a preference for some particular direction. If the two elements have this built-in preference, they can act as nucleation centers of eventually opposite toroidal order, being another eventual source for domain structure. Looking at the type of domain walls in Fig. 6 we note that diagonal domain walls are more frequent than vertical and horizontal. It indicates that the interactions between the unit cells are stronger than the interactions within the unit cells [11]. The eventual enlargement of the domain sizes can probably be reached by a slight enlargement of the gaps between cells to set up intra- and inter-cell interactions at the same level [11].

VI. CONCLUSION

In summary, we suggest a new magnetization protocol for achieving ferrotoroic order based on spontaneous symmetry breaking. As demonstrated by the macrospin model, the field-free unit-cell ground state has the lowest eigenenergy and is the first to break the symmetry when the out-of-plane magnetic field is reduced. The external out-of-plane magnetic field can be set up to a value in some interval when the only stable magnetic state of the unit cell is toroidal. The array of unit cells can be ordered into domains with ferrotoroidal states under these conditions. The external field does not have any ordering effect itself; it just lowers the energy barriers among possible states and destabilizes non-toroidal states in unit cells. The lowering of energy barriers by a magnetic field allows annealing of the magnetic order with temperatures lower than the Curie temperature of the constituting material. Lowering the energy barriers and destabilization of meta-stable states is probably more general and applicable also to other structures facilitating annealing of magnetic structures towards the ground state.

ACKNOWLEDGMENT

We acknowledge the financial support to Slovak grant agency VEGA through projects No. 2/0168/24 and No. 2/0168/22. The contribution of P.B. was supported by the Slovak Research and Development Agency, Slovakia under the contract No. APVV-22-0115.

- D. R. Smith, J. B. Pendry, and M. C. Wiltshire, Metamaterials and negative refractive index, Science 305, 788 (2004).
- [2] J. B. Pendry, D. Schurig, and D. R. Smith, Controlling electromagnetic fields, Science 312, 1780 (2006).
- [3] C. Ederer and N. A. Spaldin, Towards a microscopic theory of toroidal moments in bulk periodic crystals, Physical Review B—Condensed Matter and Materials Physics 76, 214404 (2007).
- [4] H. Schmid, Some symmetry aspects of ferroics and single phasemultiferroics, Journal of Physics: Condensed Matter 20, 434201 (2008).
- [5] N. A. Spaldin, M. Fiebig, and M. Mostovoy, The toroidal moment in condensed-matter physics and its relation to the magnetoelectriceffect, Journal of Physics: Condensed Matter 20, 434203 (2008).
- [6] A. S. Zimmermann, D. Meier, and M. Fiebig, Ferroic nature of magnetic toroidal order, Nature communications 5, 4796 (2014).
- [7] R. Shindou, J.-i. Ohe, R. Matsumoto, S. Murakami, and E. Saitoh, Chiral spin-wave edge modes in dipolar magnetic thin films, Physical Review B—Condensed Matter and Materials Physics 87, 174402 (2013).
- [8] J. Feilhauer, M. Zelent, Z. Zhang, J. Christensen, and M. Mruczkiewicz, Unidirectional spin-wave edge modes in magnonic crystal, APL Materials 11 (2023).
- [9] J. P. Morgan, A. Stein, S. Langridge, and C. H. Marrows, Thermal ground-state ordering and elementary excitations in artificial magnetic square ice, Nature Physics 7, 75 (2011).
- [10] J. Lehmann, C. Donnelly, P. M. Derlet, L. J. Heyderman, and M. Fiebig, Poling of an artificial magneto-toroidal crystal, Nature nanotechnology 14, 141 (2019).
- [11] J. Lehmann, A. Bortis, P. M. Derlet, C. Donnelly, N. Leo, L. J. Heyderman, and M. Fiebig, Relation between microscopic interactions and macroscopic properties in ferroics, Nature nanotechnology 15, 896 (2020).
- [12] J. Lehmann, Toroidal Order in Magnetic Metamaterials (Springer Nature, 2021).
- [13] J. Lehmann, N. Leo, L. J. Heyderman, and M. Fiebig, Long-range order in arrays of composite and monolithic magnetotoroidal moments, Physical Review B 108, 104405 (2023).
- [14] W.-C. Yue, Z. Yuan, P. Huang, Y. Sun, T. Gao, Y.-Y. Lyu, X. Tu, S. Dong, L. He, Y. Dong, et al., Toroidic phase transitions in a direct-kagome artificial spin ice, Nature Nanotechnology, 1 (2024).

- [15] T. Ščepka, J. Feilhauer, J. Tóbik, S. Krylov, T. Kalmykova, V. Cambel, and M. Mruczkiewicz, Control of closure domain state circulation in coupled triangular permalloy elements using mfm tip, Journal of Applied Physics 134 (2023).
- [16] V. Schánilec, B. Canals, V. Uhlíř, L. Flajšman, J. Sadílek, T. Šikola, and N. Rougemaille, Bypassing dynamical freezing in artificial kagome ice, Physical Review Letters 125, 057203 (2020).
- [17] V. Schánilec, O. Brunn, M. Horáček, S. Krátkỳ, P. Meluzín, T. Šikola, B. Canals, and N. Rougemaille, Approaching the topological low-energy physics of the f model in a two-dimensional magnetic lattice, Physical Review Letters 129, 027202 (2022).
- [18] W. Hu, K. Sarveswaran, M. Lieberman, and G. H. Bernstein, Sub-10 nm electron beam lithography using cold development of poly (methylmethacrylate), Journal of Vacuum Science & Technology B: Microelectronics and Nanometer Structures Processing, Measurement, and Phenomena 22, 1711 (2004).
- [19] T. Inui, Y. Tanabe, and Y. Onodera, Group theory and its applications in physics, Vol. 78 (Springer Science & Business Media, 2012).
- [20] The four eigenvectors $\mathbf{u}_7, ..., \mathbf{u}_{10}$ are parametrized by interaction constants A, J, and their explicit form is $\mathbf{u}_7 = (A + \sqrt{A^2 + 16J^2})/(4J)\mathbf{e}_7 + \mathbf{e}_9,$ $\mathbf{u}_8 = -(A + \sqrt{A^2 + 16J^2})/(4J)\mathbf{e}_8 + \mathbf{e}_{10}, \mathbf{u}_9 = (A \sqrt{A^2 + 16J^2})/(4J)\mathbf{e}_7 + \mathbf{e}_9, \mathbf{u}_{10} = (-A + \sqrt{A^2 + 16J^2})/(4J)\mathbf{e}_8 + \mathbf{e}_{10}).$
- [21] A. Laio and M. Parrinello, Escaping free-energy minima, Proceedings of the national academy of sciences 99, 12562 (2002).
- [22] J. Tóbik, R. Martoňák, and V. Cambel, Free-energy landscapes in magnetic systems from metadynamics, Physical Review B 96, 140413 (2017).
- [23] I. Charalampidis and J. Barker, Metadynamics calculations of the effect of thermal spin fluctuations on skyrmion stability (2023), arXiv:2310.03169 [condmat.mtrl-sci].
- [24] A. Barducci, G. Bussi, and M. Parrinello, Well-tempered metadynamics: A smoothly converging and tunable freeenergy method, Phys. Rev. Lett. 100, 020603 (2008).
- [25] S. Lepadatu, Boris computational spintronics—high performance multi-mesh magnetic and spin transport modeling software, Journal of Applied Physics 128 (2020).
- [26] S. Lepadatu, Boris2 (2024), Computer program. Available at: https://github.com/SerbanL/Boris2 (Accessed: 2025-09-03).

- [27] S. Lepadatu, Micromagnetic monte carlo method with variable magnetization length based on the landau– lifshitz-bloch equation for computation of large-scale thermodynamic equilibrium states, Journal of Applied Physics 130 (2021).
- [28] S. Lepadatu, Accelerating micromagnetic and atomistic simulations using multiple gpus, Journal of Applied Physics 134 (2023).
- [29] S. Lepadatu, G. Mckenzie, T. Mercer, C. R. MacKinnon, and P. R. Bissell, Computation of magnetization, exchange stiffness, anisotropy, and susceptibilities in largescale systems using gpu-accelerated atomistic parallel
- monte carlo algorithms, Journal of Magnetism and Magnetic Materials **540**, 168460 (2021).
- [30] M. Fiebig, private communication (2024), we acknowledge this point was brought to us via e-mail communication.
- [31] M. Schneider, H. Hoffmann, and J. Zweck, Magnetic switching of single vortex permalloy elements, Applied Physics Letters 79, 3113 (2001).
- [32] J. Tóbik, Dynamical symmetry breaking in magnetic systems, physica status solidi (RRL)-Rapid Research Letters 17, 2200459 (2023).